Impact of the pairing interaction on fission of U isotopes

Xin Guan,[1,*] Tian-Cong Wang,[1] Wan-Qiu Jiang,[1] Yang Su,[2] Yong-Jing Chen,[2] and Krzysztof Pomorski[3]
[1]*Department of Physics, Liaoning Normal University, Dalian 116029, China*
[2]*China Nuclear Data Center, China Institute of Atomic Energy, Beijing 102413, China*
[3]*Institute of Physics, Maria Curie Skłodowska University, 20-031 Lublin, Poland*

(Received 17 November 2022; accepted 28 February 2023; published 14 March 2023)

The role of pairing interactions on the scission configurations, the total kinetic energy, and the mass distributions in U isotopes is investigated using the deformed mean-field plus standard pairing model. The total kinetic energy and the mass distributions of $^{232-238}$U isotopes obtained using the shape-dependent probability distribution expressed by the Wigner function reproduces the experimental data remarkably well. The model calculations show that the scission region is sensitive to the variation of the pairing interaction strength, particularly for the asymmetric and symmetric scission points. The apparent changes in the peak-to-valley ratio in mass distribution by varying the pairing interaction strength confirm that the pairing interaction plays an important role in achieving the scission process for ^{236}U under the present model. These results also suggest that the pairing interaction strength in the current work should increase with the elongation of the nucleus to yield better fission products. Through numerical analysis, we provide possible microscopic pictures of spontaneous fission around the scission configurations in the exactly solvable pairing model.

DOI: 10.1103/PhysRevC.107.034307

I. INTRODUCTION

Despite decades of research in nuclear fission, there are still several open questions about this complex reaction process, and a deeper understanding of the fission mechanism is strongly motivated [1–6]. The final state in nuclear fission is the neck rupture between the two nascent fragments, leaving them to interact only through long-range potential fields. The quantum dynamics of this scission process is pretty complex and has been discussed many times [7–13]. In recent work, the new technique directly determines the evolution of the scissioned shape distribution according to the number of random-walk steps rather than the statistical accumulation of fission events [14]. One should emphasize that the physics of scission remains poorly known. How fission fragments acquire their identity and the connection of this process with the physics of quantum entanglement has not been studied.

As one of the dominant residual correlations in atomic nuclei, pairing interaction around the scission point is crucial to understand many aspects of the final fission state, including, for example, the total kinetic energy (TKE) distribution of the fragments and the odd-even effects in mass distributions [15–17]. The macroscopic-microscopic studies have demonstrated that pairing fluctuations can significantly reduce collective action and can affect the predicted spontaneous fission lifetimes [18]. The BCS approximation and the generalized Hartree-Fock-Bogoliubov (HFB) approach have been used to describe the pairing properties. It has also shown the dynamical coupling between shape and pairing degrees of freedom can lead to a dramatic departure from the static picture [7]. Based on the density-functional theory (DFT), calculations in Refs. [19,20] have shown that increasing pairing correlations decrease the fission barrier and lead to scission occurring at lower elongations. The collective inertia strongly depends on the pairing gap [21,22]. The inertia is inversely proportional to the square of the pairing gap parameter, and the larger pairing gaps imply a smaller inertia. Therefore, this leads to shorter fission half-lives [23–27]. The analysis of the dynamical description of nuclear fission based on the density-functional theory (DFT) showed that the particle-particle correlations should be considered on the same footing as those associated with the shape degrees of freedom [28]. Recent theoretical works based on the time-dependent Hartree-Fock method have shown that fission could also be very sensitive to nongeometric collective variables such as pairing correlations. For instance, Sadhukhan *et al.* demonstrated that the inclusion of pairing collective degrees of freedom had a significant impact on the spontaneous fission half-lives of ^{264}Fm and ^{240}Pu [29]. The study of the compound nucleus ^{240}Pu displays that the dynamical pairing is vanishing at high excitations. For driving fission, the random transition between single-particle levels around the Fermi surface to mimic thermal fluctuations is indispensable [30]. Using the relativistic energy density functionals, the induced fission of ^{226}Th was investigated [31]. It showed that increasing static pairing interactions reduces the asymmetric peaks and enhances the symmetric peak in the charge distribution. Also, the fission-fragment yields are characterized by several components in the mass distributions from different fission channels. This is attributed to shell effects in the potential energy and an odd-even staggering in proton and neutron numbers due to the influence of pairing interactions. [32].

*guanxin@lnnu.edu.cn

In the current work, based on an iterative algorithm [33,34], we have investigated the fission barriers and the static fission path in Th, U, and Pu isotopes based on the deformed mean-field plus standard pairing model with the exact pairing solution. It indicates that the pairing interaction plays different roles in different stages of the fission process. The first and second saddle points are very sensitive to the variation of the pairing interaction strength [35]. The systematic investigation of the inner and outer fission barriers of even-even nuclei Th, U, and Pu isotopes shows that the standard pairing model reproduces the inner and outer barrier heights considerably closer to the experiment than the BCS scheme. The results display that the standard pairing model can be applied to study the static and dynamic properties of the fissioning system. However, the deformed-shape description in Ref. [35] cannot be applied to the configuration corresponding to the separated fragments and to the physics of scission. The role of the pairing interaction around the scission point is still far from clear. In particular, the effect of the dynamical coupling between shape and pairing interactions on the scission configurations and the mass distributions of fission fragments has yet to be resolved. Furthermore, based on the DFT with BCS pairing theory, the results in Ref. [19] suggest that a predictive theory of nuclear fission will require a very accurate description of pairing correlations. Therefore, exploring possible mechanisms with the exactly solvable pairing model is essential to account for the scission configurations and mass distributions. Recently, it has been observed that the developed Fourier parametrization of deformed nuclear shapes is very efficient at describing the essential features of the shapes involved up to the scission configuration [36,37]. The Fourier shape parametrization combined with the Lublin-Strasbourg drop (LSD) + Yukawa-folded single-particle potential was used in studying the dynamical process of nuclear fission by using a Langevin approach [38]. The calculated fragment mass distributions and TKE distributions in 14 MeV $n + {}^{233,235,236,238}$U and ^{239}Pu fission agree with experimental data. The correlation between the deformation parameters at the scission point is studied as well. These studies have provided a valid model to investigate the fission properties of the scission configurations.

This work systematically analyzes the scission configurations, the mean value of total kinetic energy, and the mass distributions in U isotopes within the deformed mean-field plus standard pairing model. The potential energy is calculated under the macroscopic-microscopic framework. The Fourier shape parametrization combined with the LSD model + Yukawa-folded potential has been used in the current calculations. As an extension of our previous work in Ref. [35], the role of the pairing interaction on the scission configurations and mass distributions will also be addressed.

II. THEORETICAL FRAMEWORK AND NUMERICAL DETAILS

A. Deformed mean-field plus standard pairing model

The Hamiltonian of the deformed mean-field plus standard pairing model for either the proton or the neutron sector is given by

$$\hat{H} = \sum_{i=1}^{n} \varepsilon_i \hat{n}_i - G \sum_{ii'} S_i^+ S_{i'}^-, \tag{1}$$

where the sums run over all given i-double degeneracy levels of total number n, $G > 0$ is the overall pairing interaction strength, $\{\varepsilon_i\}$ are the single-particle energies obtained from mean-field, such as Hartree-Fock (HF), Woods-Saxon potential (WS), Yukawa-folded single-particle potential, or Nilsson model. $n_i = a_{i\uparrow}^\dagger a_{i\uparrow} + a_{i\downarrow}^\dagger a_{i\downarrow}$ is the fermion number operator for the ith double degeneracy level, and $S_i^+ = a_{i\uparrow}^\dagger a_{i\downarrow}^\dagger$ [$S_i^- = (S_i^+)^\dagger = a_{i\downarrow} a_{i\uparrow}$] is the pair creation (annihilation) operator, The up and down arrows in these expressions refer to time-reversed states.

According to the Richardson-Gaudin method [39–42], the exact k-pair eigenstates of (1) with $\nu_{i'} = 0$ for even systems or $\nu_{i'} = 1$ for odd systems, in which i' is the label of the double degeneracy level that is occupied by an unpaired single particle can be written as

$$|k;\xi;\nu_{i'}\rangle = S^+\big(x_1^{(\xi)}\big) S^+\big(x_2^{(\xi)}\big) \cdots S^+\big(x_k^{(\xi)}\big) |\nu_{i'}\rangle, \tag{2}$$

where $|\nu_{i'}\rangle$ is the pairing vacuum state with the seniority $\nu_{i'}$ that satisfies $S_i^-|\nu_{i'}\rangle = 0$ and $\hat{n}_i|\nu_{i'}\rangle = \delta_{ii'}\nu_i|\nu_{i'}\rangle$ for all i. Here, ξ is an additional quantum number for distinguishing different eigenvectors with the same quantum number k and

$$S^+\big(x_\mu^{(\xi)}\big) = \sum_{i=1}^{n} \frac{1}{x_\mu^{(\xi)} - 2\varepsilon_i} S_i^+, \tag{3}$$

in which the spectral parameters $x_\mu^{(\xi)}$ ($\mu = 1, 2, \ldots, k$) satisfy the following set of Bethe ansatz equations (BAEs):

$$1 + G \sum_i \frac{\Omega_i}{x_\mu^{(\xi)} - 2\varepsilon_i} - 2G \sum_{\mu'=1\ (\neq\mu)}^{k} \frac{1}{x_\mu^{(\xi)} - x_{\mu'}^{(\xi)}} = 0, \tag{4}$$

where the first sum runs over all i levels and $\Omega_i = 1 - \delta_{ii'}\nu_{i'}$. For each solution, the corresponding eigenenergy is given by

$$E_k^{(\xi)} = \sum_{\mu=1}^{k} x_\mu^{(\xi)} + \nu_{i'}\varepsilon_{i'}. \tag{5}$$

In general, according to the polynomial approach in Refs. [43–45], one can find solutions of Eq. (4) by solving the second-order Fuchsian equation [46] as

$$A(x)P''(x) + B(x)P'(x) - V(x)P(x) = 0, \tag{6}$$

where $A(x) = \prod_{i=1}^{n}(x_\mu^{(\xi)} - 2\varepsilon_i)$ is an n-degree polynomial,

$$B(x)/A(x) = -\sum_{i=1}^{n} \frac{\Omega_i}{x_\mu^{(\xi)} - 2\varepsilon_i} - \frac{1}{G}, \tag{7}$$

$V(x)$ are called Van Vleck polynomials [46] of degree $n-1$, which are determined according to Eq. (6). They are defined as

$$V(x) = \sum_{i=0}^{n-1} b_i x^i. \tag{8}$$

The polynomials $P(x)$ with zeros corresponding to the solutions of Eq. (4) is defined as

$$P(x) = \prod_{i=1}^{k} \left(x - x_i^{(\xi)}\right) = \sum_{i=0}^{k} a_i x^i, \tag{9}$$

where k is the number of pairs. b_i and a_i are the expansion coefficients to be determined instead of the Richardson variables x_i. Furthermore, if we set $a_k = 1$ in $P(x)$, the coefficient a_{k-1} then equals the negative sum of the $P(x)$ zeros, $a_{k-1} = -\sum_{i=1}^{k} x_i^{(\xi)} = -E_k^{(\xi)}$.

If the value of x approaches twice the single-particle energy of a given level δ, i.e., $x = 2\varepsilon_\delta$, one can rewrite Eq. (6) in doubly degenerate systems with $\Omega_i = 1$ as [43,45]

$$\left(\frac{P'(2\varepsilon_\delta)}{P(2\varepsilon_\delta)}\right)^2 - \frac{1}{G}\left(\frac{P'(2\varepsilon_\delta)}{P(2\varepsilon_\delta)}\right) = \sum_{i\neq\delta} \frac{\left[\left(\frac{P'(2\varepsilon_\delta)}{P(2\varepsilon_\delta)}\right) - \left(\frac{P'(2\varepsilon_i)}{P(2\varepsilon_i)}\right)\right]}{2\varepsilon_\delta - 2\varepsilon_i}. \tag{10}$$

In Ref. [33], a new iterative algorithm is established for the exact solution of the standard pairing problem within the Richardson-Gaudin method using the polynomial approach in Eq. (10). It provides efficient and robust solutions for both spherical and deformed systems at a large scale. The key to its success is determining the initial guesses for the large-set nonlinear equations involved in a controllable and physically motivated manner. Moreover, one reduces the large-dimensional problem to a one-dimensional Monte Carlo sampling procedure, which improves the algorithm's efficiency and avoids the nonsolutions and numerical instabilities that persist in most existing approaches. Based on the new iterative algorithm, we applied the model to study the actinide nuclei isotopes, where an excellent agreement with experimental data was obtained [33–35].

B. The Fourier shape parametrization

In the macroscopic-microscopic approach, the potential-energy surface (PES) is a function of all the parameters needed to describe the nuclear shape. How to precisely describe the nuclear shapes, especially in connection with fission, involving as few variables as possible is a demanding task. Numerous parametrizations have been introduced over the years, and several powerful shape parametrizations have been developed [47]. In Ref. [36], the nuclear shape is described by using the Fourier shape parametrization, which can cover a wide variety of shapes with only four collective deformation parameters. The current works show that the innovative Fourier parametrization of nuclear shapes, combined with LSD + Yukawa-folded macroscopic-microscopic potential-energy prescription turns out to be very efficient [36,38]. The macroscopic-microscopic framework given in Ref. [36] will be mainly adopted in this work, in which the single-particle energies $\{\varepsilon_i\}$ in the model Hamiltonian (1) are obtained from the Yukawa-folded. The expansion of the nuclear surface in the form of the Fourier series of dimensionless coordinates is as follows:

$$\frac{\rho_s^2(z)}{R_0^2} = \sum_{n=1}^{\infty}\left[a_{2n}\cos\left(\frac{(2n-1)\pi}{2}\frac{z-z_{\rm sh}}{z_0}\right) + a_{2n+1}\sin\left(\frac{2n\pi}{2}\frac{z-z_{\rm sh}}{z_0}\right)\right], \tag{11}$$

where $\rho_s^2(z)$ is the distance from a surface point to the symmetry z axis, and $R_0 = 1.2A^{1/3}$ fm is the radius of the corresponding spherical shape having the same volume. The extension of the shape along the symmetry axis is $2z_0$ with left and right ends located at $z_{\rm min} = z_{\rm sh} - z_0$ and $z_{\rm max} = z_{\rm sh} + z_0$, respectively. z_0 is the half of the extension of the shape along the symmetry axis, which can be obtained from the volume conservation, and $z_{\rm sh}$ is determined by imposing the condition that the center of mass of the nuclear shape is located at the origin of the coordinate system. According to the convergence properties discussed in Ref. [37], the first five orders $a_2, \ldots, a_6$ were retained here as a starting point and the parameters a_n are transformed to the deformation parameters q_n as follows, respectively:

$$\begin{aligned}
q_2 &= a_2^{(0)}/a_2 - a_2/a_2^{(0)},\\
q_3 &= a_3,\\
q_4 &= a_4 + \sqrt{(q_2/9)^2 + \left(a_4^{(0)}\right)^2},\\
q_5 &= a_5 - (q_2 - 2)\,a_3/10,\\
q_6 &= a_6 - \sqrt{(q_2/100)^2 + \left(a_6^{(0)}\right)^2},
\end{aligned} \tag{12}$$

where $a_n^{(0)}$ are the values of the Fourier coefficients for the spherical shape. The higher-order coordinates q_5 and q_6 are generally set to be zero within the accuracy of the current approach. It indicates that the set of q_i has explicit physical meaning in describing the shape of the fissioning nucleus, i.e., q_2 denotes the elongation of the nucleus, q_4 is the neck parameter, and q_3 is the left-right asymmetry parameter. In this work, the dynamic process of nuclear fission will be described in the three-dimensional deformation space $(q_2, q_3; q_4)$ within the Fourier shape parametrization. It should be noted that the nonaxially symmetric shape is not taken into account in the present work since it plays an important role only in the vicinity of the ground state and the first saddle point.

C. The mass and total kinetic-energy distribution

It has been observed recently [37,48–50] that a Wigner function is used to approximate the probability distribution related to the neck and mass asymmetry degrees of freedom. It is shown that the agreement of this model's predictions with the experimental yields is pretty good [51]. Based on the previous works [37,48–50], the fundamental idea of the fission dynamics discussed in this work is that the relatively slow motion towards fission, mainly in q_2 direction, is accompanied by the fast vibrations in the perpendicular q_3 and q_4 collective variables. The wave function corresponding to the total eigenvalue E of the fissioning nucleus approximately as

$$\psi_{nE}(q_2, q_3, q_4) = \mu_{nE}(q_2)\phi_n(q_3, q_4; q_2). \tag{13}$$

Here, $\mu_{nE}(q_2)$ is the eigenfunction corresponding to the motion towards fission, which depends mainly on a single variable q_2. $\phi_n(q_3, q_4; q_2)$ simulates the n-phonon fast collective vibrations on the perpendicular two-dimensional (2D) $\{q_3, q_4\}$ plane for a given elongation q_2. For $\mu_{nE}(q_2)$ one can use the Wenzel-Kramers-Brillouin (WKB) approximation for a single q_2 mode [49]. For low-energy fission, only the lowest energy eigenstate $\phi_{n=0}$ is considered.

The density of probability $W(q_3, q_4; q_2)$ of finding the system for a given elongation q_2,within the area of $(q_3 \pm dq_3, q_4 \pm dq_4)$, is given as

$$W(q_3, q_4; q_2) = |\psi(q_2, q_3, q_4)|^2 = |\phi_0(q_3, q_4; q_2)|^2. \quad (14)$$

Instead of the square of the collective wave function in Eq. (14), we take the following Wigner function:

$$W(q_3, q_4; q_2) \propto \exp\left\{-\frac{\mathrm{V(q_3, q_4; q_2)} - \mathrm{V_{min}(q_2)}}{\mathrm{E_0}}\right\}, \quad (15)$$

where $V_{\min}(q_2)$ is the minimum of the potential for a given elongation q_2, and E_0 is the zero-point energy, which is treated as an adjustable parameter.

To obtain the fragment mass yield for a given elongation q_2, one has to integrate the probabilities (15) coming from different neck shapes, simulated basically by the q_4 parameter

$$w(q_3; q_2) = \int W(q_3, q_4; q_2) dq_4. \quad (16)$$

Following the idea in Ref. [49], one assumes the neck rupture probability P to be equal to

$$P(q_3, q_4, q_2) = \frac{k_0}{k} P_{\mathrm{neck}}(R_{\mathrm{neck}}), \quad (17)$$

where k is the momentum in the direction towards fission and the constant parameter k_0 plays the role of scaling parameter. R_{neck} is the deformation-dependent neck radius, and P_{neck} is a geometrical factor indicating the neck-breaking probability proportional to the neck thickness. The expression for the geometrical probability factor $P_{\mathrm{neck}}(R_{\mathrm{neck}})$ can be chosen arbitrarily to some extent, such as, e.g., Fermi, Lorentz, and Gaussian functions [50]. In this paper, we used the Gaussian form as follows:

$$P_{\mathrm{neck}}(R_{\mathrm{neck}}) = \exp[-\ln 2(\mathrm{R_{neck}/d})^2], \quad (18)$$

where d is the half-width of the probability, treated here as another adjustable parameter. The momentum k in Eq. (17) simulates the dynamics of the fission process, which, as usual, depends both on the local collective kinetic energy $E - V(q2)$ and the inertia towards the leading variable q_2

$$\frac{\hbar^2 k^2}{2\overline{M}(q_2)} = E_{\mathrm{kin}} = E - Q - V(q_2), \quad (19)$$

where $\overline{M}(q_2)$ standing for the averaged inertia parameter over q_3 and q_4 degrees of freedom at a given elongation q_2, and $V(q_2)$ is the averaged potential. Here, the part of the total energy converted into heat Q is assumed to be negligibly small. A good approximation of the inertia $\overline{M}(q_2)$ is to use the irrotational flow mass parameter B_{irr} [52], which is derived initially as a function of the single collective parameter R_{12}, the distance between fragments, and the reduced mass μ of both fragments

$$\overline{M}(q_2) = \mu[1 + 11.5(B_{\mathrm{irr}}/\mu - 1)]\left(\frac{\partial R_{12}}{\partial q_2}\right)^2. \quad (20)$$

To make use of the neck rupture probability $P(q_3, q_4; q_2)$ in Eq. (17), one has to rewrite the integral over q_4 probability distribution in Eq. (15) in the form of

$$w(q_3; q_2) = \int W(q_3, q_4; q_2) P(q_2, q_3, q_4) dq_4. \quad (21)$$

The above approximation implies a very crucial fact that, for a fixed q_3 value, the fission may occur within a certain range of q_2 deformations with different probabilities. Therefore, to obtain the true fission probability distribution $w'(q_3; q_2)$ at a strictly given q_2, one has to exclude the fission events occurred in the previous $q_2' < q_2$ configurations, i.e.,

$$w'(q_3; q_2) = w(q_3; q_2) \frac{1 - \int_{q_2' < q_2} w(q_3; q_2') dq_2'}{\int w(q_3; q_2') dq_2'}. \quad (22)$$

The normalized mass yield is then obtained as the sum of partial yields at different given q_2:

$$Y(q_3) = \frac{\int w'(q_3; q_2) dq_2}{\int w'(q_3; q_2) dq_3 dq_2}. \quad (23)$$

Since the scaling parameter k_0 introduced in Eq. (17) does not longer appear in the definition of the mass yield, the only free parameters, the zero-point energy parameter E_0 in Eq. (14) and the half-width parameter d appear in the probability of neck rupture (18). In this work, we follow the parameter $d = 0.15R_0$ in Ref. [37], which has been successfully reproduced the experimental fragment mass yields measured in the low-energy fission of Pt to Ra isotopes, and the zero-point energy parameter $E_0 = 1.5$ MeV.

D. The potential energy

In Ref. [35], we systematically analyzed fission barriers and static fission paths in Th, U, and Pu isotopes within the deformed mean-field plus standard pairing model, which indicates that the pairing interaction plays different roles in different stages of the fission processes. That results encouraged us to investigate the possible impact of pairing interactions in the scission configuration and on the mass distribution for the low-energy fission of U isotopes. The potential energy of the system is calculated within the macroscopic-microscopic approach in this work. The total energy $E_{\mathrm{total}}(N, Z, q_n)$ of a nucleus with a given deformation is calculated as

$$E_{\mathrm{total}}(N, Z, q_n) = E_{\mathrm{LD}}(N, Z) + E_{\mathrm{B}}(N, Z, q_n), \quad (24)$$

where $E_{\mathrm{LD}}(N, Z)$ is the macroscopic term approximated by the standard liquid drop model with proton number Z and neutron number N [53]. In the current calculation for the potential-energy surface, we just consider the energy $E_{\mathrm{B}}(N, Z, q_n)$ related to the shape parameter $\{q_2, q_3, q_4\}$:

$$E_{\mathrm{B}}(N, Z, q_n) = E_{\mathrm{def}}(N, Z, q_n) + E_{\mathrm{shell}}(N, Z, q_n) + E_{\mathrm{pair}}(N, Z, q_n). \quad (25)$$

In this work, the deformation correction energy $E_{\rm def}(N, Z, q_2, q_3, q_4)$ is taken from tables of Ref. [54]. The microscopic term consists of the shell correction energy $E^{\nu(\pi)}_{\rm shell}(N, Z, \{\varepsilon_i\}, q_2, q_3, q_4)$ proposed by Strutinsky [55,56] and the pairing interaction energy $E^{\nu(\pi)}_{\rm pair}(N, Z, \{\varepsilon_i\}, q_2, q_3, q_4)$ calculated from Eq. (1). Here, ν (π) is the label of the neutron (proton) sector. In the current study, we consider 18 deformed harmonic-oscillator shells in Yukawa-folded single-particle potential to obtain single-particle levels for the microscopic calculations. For the pairing correction energy, we perform 66 single-particle levels around the neutron Fermi level and 51 single-particle levels around the proton Fermi level. The multidimensional potential-energy surface is minimized simultaneously in all axial degrees of freedom: elongation of the nucleus q_2, asymmetry of left and right mass fragments q_3, and the neck size q_4.

Generally, the pairing interaction strength G is determined by the empirical formula or by fitting the odd-even mass differences [57,58]. The recent study [35,59] reveals that pairing interactions play a crucial role in the regions of the inner and outer barriers, the first and second saddle points are sensitive to the variation of the pairing interaction strength. Therefore, the odd-even mass differences (ground-state property) and the height of barriers (excited-state property) should be used as experimentally observable quantities to determine the realistic values for pairing interaction strength in the fission process. In this work, realistic values of pairing interaction strengths for U isotopes are obtained by fitting the experimental values of the odd-even mass differences and the inner and outer barriers. The odd-even mass difference is given by

$$P(A) = E_{\rm total}(N+1, Z) + E_{\rm total}(N-1, Z) - 2E_{\rm total}(N, Z), \tag{26}$$

which is usually attributed to the existence of nucleonic pairing interactions. It is sensitive to the changes in the pairing interaction strength G [60]. When the pairing interaction strength $G^{\nu} = 0.08$ MeV and $G^{\pi} = 0.10$ MeV, it is clearly shown in Fig. 1(a) that odd-even mass differences obtained by using the present approach reproduce the experimental data remarkably well for the $^{224-238}$U isotopes. Moreover, as shown in Figs. 1(b) and 1(c), the results of the inner and outer fission barriers for $^{231-240}$U isotopes calculated in the current model are very close to the corresponding experimental values.

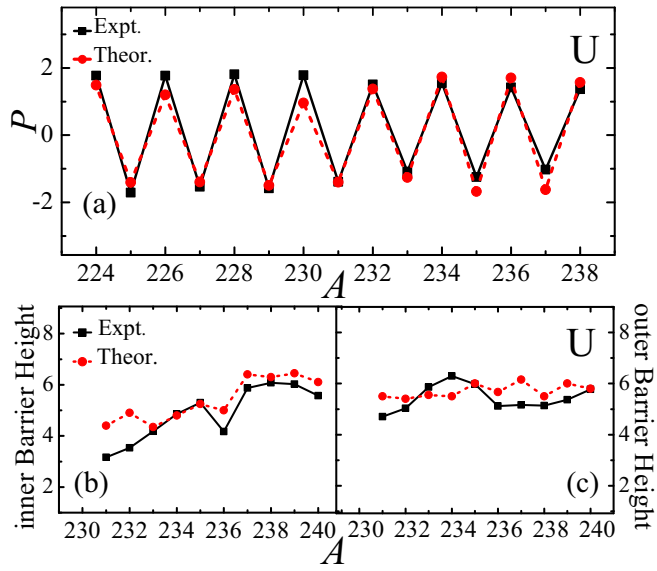

FIG. 1. The odd-even mass differences (in MeV), inner and outer fission barriers heights for U isotopes. Experimental values are denoted as "Expt." and the theoretical values calculated in the present model are denoted as "Theor." Experimental data are taken from Refs. [60,61] (in MeV). A typical uncertainty in the experimental values, as suggested by the differences among various compilations, is of the order of 0.5 MeV [61].

III. RESULTS AND DISCUSSIONS

A. The role of pairing around the scission

First, for investigating the microscopic mechanism of the interplay between the pairing interaction and the deformation of the scission configuration under the present model, the three-dimensional (3D) contour map of the potential-energy surface (PES) of the nucleus ^{236}U is projected in Fig. 2 constrained by the elongation parameter q_2, the octupole deformation parameters q_3 and minimized the degree of freedom q_4.

As shown in Fig. 2, at the beginning of the fission process $q_2 < 0.5$, the PES displays very soft octupole deformation, and the minimum of the PES (ground state) is located at $q_3 = 0$. It is consistent with the analysis of the relativistic Hartree-Bogoliubov (RHB) calculations in Ref. [62]. It shows that the nucleus of the $A < 236$ for U isotopes remains in the octupole vibrational regime, and the PES of this nucleus are very soft in the q_3 direction. For the fission barrier heights,

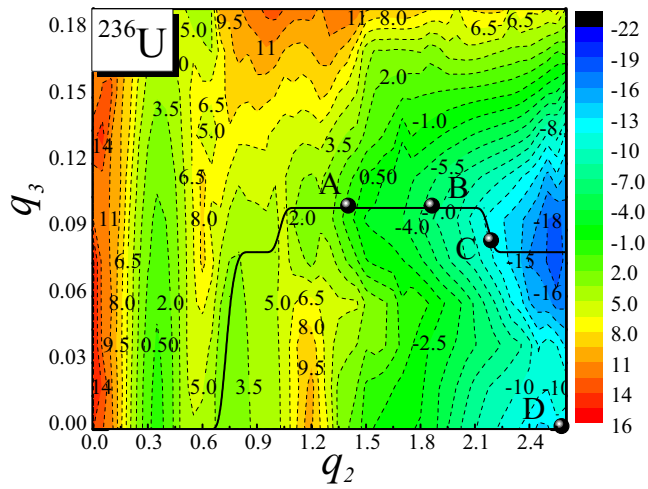

FIG. 2. Contour map of the potential-energy surface of the nucleus ^{236}U (in MeV), minimized q_4 with the pairing interaction strength $G^{\nu} = 0.08$ and $G^{\pi} = 0.10$ (in MeV). The black trajectory shows the static fission path. Positions of the prescission point, the scission process point, the asymmetric scission point, and the symmetric scission point are indicated by the black balls with the capital letters A–D.

TABLE I. The q_2, q_3, q_4 values of the four characteristic points (black points with the capital letters in Fig. 2) in the three-dimensional deformation space based on the results of the static fission path (black trajectory).

	q_2	q_3	q_4
Prescission point (A)	1.40	0.10	−0.12
Scission process point (B)	1.85	0.10	−0.12
Asymmetric scission point (C)	2.20	0.08	−0.09
Symmetric scission point (D)	2.60	0.00	−0.06

the inner barrier height is 4.57 MeV, the outer barrier height is 5.67 MeV calculated from the present model, and the corresponding experimental results in Ref. [63] are 5.0 and 5.11 MeV. The barrier heights obtained by using the present model are found to reproduce the experimental data remarkably well. In addition, it is clearly shown in Fig. 2 that there is a plateau at high deformation followed by a cliff (beyond $q_2 = 2.20$, $q_3 = 0.08$, $q_4 = -0.09$). The sudden jump at the cliff edge highlights the key point of understanding scission dynamics. The dynamics around the scission point are crucial for understanding many aspects of the final fission state, including the mass and kinetic-energy distribution of the fragments [7,8]. In this work, the scission point of the asymmetric path is determined by a fixed neck radius $R_{\rm neck}$ equal to 1.16 fm, which is close to the value (1.0 fm) adopted in Ref. [64]. To investigate the pairing interaction's role on the scission configurations, we consider the four characteristic points (black points with the capital letters in Fig. 2). The corresponding q values are shown in Table I. The points (A)–(C) are located on the asymmetric static fission path. As we discuss later, point (A) corresponds to the exit point from the fission barrier, where the fission energy shows little effect from pairing interaction. On the other hand, the scission process point (B) is associated with the position where the pairing interaction varies drastically, and the pairing interaction energy has a local minimum. The points (C) and (D) denote the asymmetric and symmetric scission point, respectively. Figure 3 describes the geometric shapes for the four characteristic points of ^{236}U within the Fourier shape parametrization. $R_{\rm neck}$ is the deformation-dependent neck radius in Eq. (17). The fission probability described by the present model should depend on the neck radius $R_{\rm neck}$. It is observed that the shape profile in Fig. 3 provides a very accurate description of the fission shapes from the prescission point to the asymmetric scission point. Following the fission process, the geometric shape is continuously elongated, the neck radius $R_{\rm neck}$ is becoming "thin," and the corresponding $R_{\rm neck}$ value decrease from 3.34 fm (the prescission point) to 1.16 fm (the asymmetric scission point). Beyond the scission point, the $R_{\rm neck}$ value will become very small ($R_{\rm neck} < 0.50$ fm) until $R_{\rm neck} = 0$, which corresponds to the totally separated fragments.

Figure 4 displays the energy curve related to the static fission path for ^{236}U with different pairing interaction strength $G^{\nu(\pi)}$ (in MeV). The ground-state energy is normalized to zero. It is clearly shown that the energy curves become lower when the original pairing interaction strengths are varied from

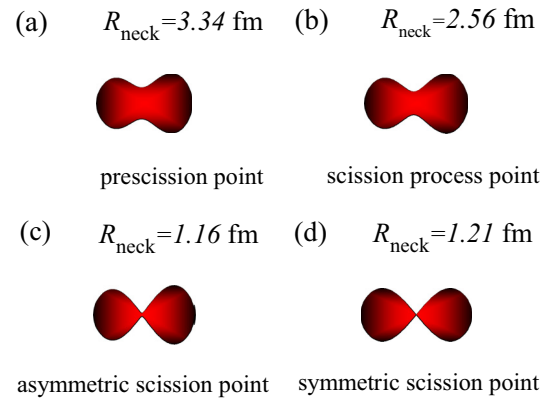

FIG. 3. Geometric shapes generated by the expansion in the Fourier series (3) of the ^{236}U for the four characteristic points. The prescission point, the scission process point, the asymmetric scission point, and the symmetric scission point are indicated by capital letters (A)–(D). $R_{\rm neck}$ is the deformation-dependent neck radius.

80% to 120%. As shown in Fig. 4, the inner and outer barrier heights decrease by increasing pairing interaction strength under the present model, which is consistent with the results obtained from our previous work [35]. The relativistic, non-relativistic mean-field + BCS framework displays the same results, too [61,65]. The second minimum ($q_2 \approx 0.75$, $q_3 \approx 0$) is much higher than the first minimum (ground state). Moreover, there is a very shallow third minimum at ($q_2 \approx 1.2$), which has been reported in Ref. [66] for U isotopes. In addition, as we mentioned before, a remarkable concurrence of the energy curves with different pairing interaction strengths occurs at $q_2 \approx 1.45$, which means the effect of pairing interaction at this point [prescission point (A)] is very weak. These results are consistent with our previous work in Ref. [35]. In contrast, beyond the prescission point $q_2 \approx 1.45$, the scission process seems more affected by the pairing interaction

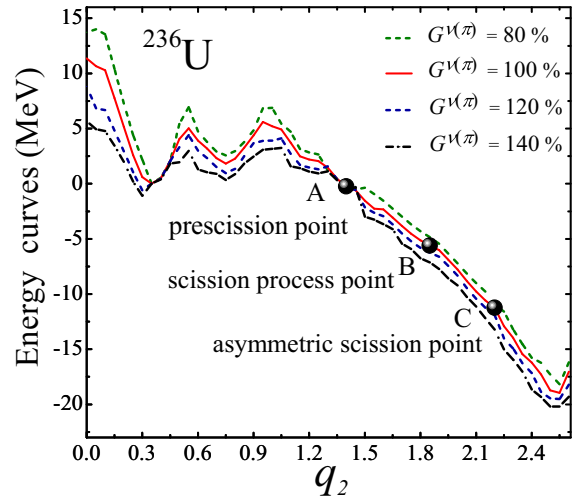

FIG. 4. The energy curves constrained by the elongation q_2 and minimized in the remaining degrees of freedom (q_3, q_4) for ^{236}U with different pairing interaction strength $G^{\nu(\pi)}$ (in MeV). Energies are normalized to zero energy at the ground-state value.

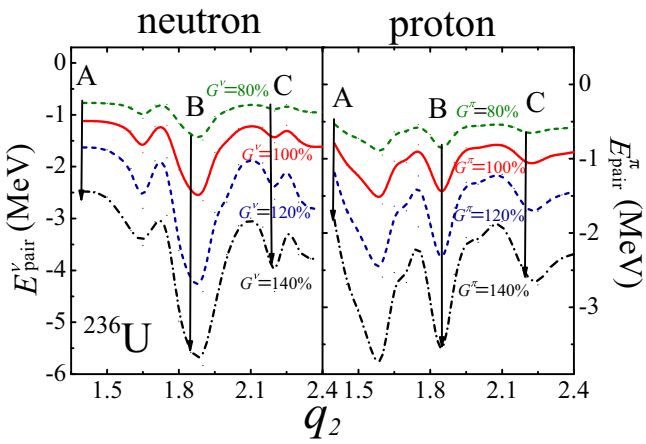

FIG. 5. Neutron and proton pairing interaction energy $E^{\nu(\pi)}_{\rm pair}$ calculated from Eq. (1), as functions of q_2 with different pairing interaction strength $G^{\nu(\pi)}$ (in MeV) for ^{236}U. (A)–(C) indicate the prescission point, the scission process point, and the asymmetric scission point, respectively. The arrows show the gap between the $E^{\nu(\pi)}_{\rm pair}$ values with different G^{ν} (G^{π}) values (in MeV).

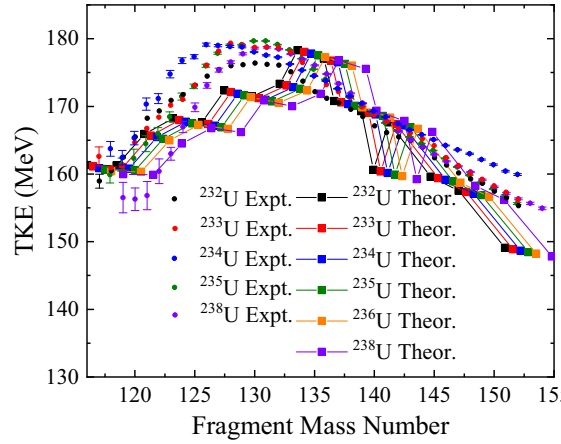

FIG. 6. The mean value of the total kinetic energy (in MeV) as a function of fragment mass for $^{232–235}$U, and ^{238}U. Experimental values are denoted as "Expt." and the theoretical values calculated in the present model are denoted as "Theor." Experimental data of neutron-induced fission are denoted as "Expt." for ^{232,233}U [68], ^{234}U [69], ^{235}U [70], and for ^{238}U [71].

strength in the present work. These results encourage us to explore the possible impacts of the pairing interaction in the scission region for ^{236}U. To elaborate more on this behavior of pairing interaction, the pairing interaction energy $E^{\nu(\pi)}_{\rm pair}$ along the asymmetric scission process from $q_2 = 1.2$ to $q_2 = 2.6$ in Fig. 4, with different pairing interaction strengths with G^{ν} (G^{π}) varied from 80% to 140% have been studied in Fig. 5. It is shown that the magnitudes of the pairing interaction energies at the scission process point (B) and at the asymmetric scission point (C) grow faster than at the prescission point (A) with the variation of the pairing interaction strength, which is consistent with the result obtained from Fig. 4. As we mentioned above, the total pairing interaction energy has a local minimum at the scission process point (B). Those results agree with the analysis in Refs. [8,19], which demonstrate that pairing interaction plays different roles in the different stages of the scission process. The scission process (B) and asymmetric scission point (C) seem much more sensitive to the pairing interaction strength G variation than the prescission point (A).

Nuclear fission is a process through which the initial compound nucleus divides predominantly into two fragments. The problem of neck rupture between nascent fragments has been discussed many times [7,8,14,19]. Any theoretical description or simulation of nuclear scission inevitably requires defining the condition under which scission occurs. In the adiabatic approximation, it is necessary to invoke reasonable physics-based arguments to justify introducing scission configurations before the fragments are far apart. The total kinetic energy, which is extremely sensitive to the characteristics of scission configurations, seems suitable to prove the definition of scission configurations [67].

In this work, the scission point for the asymmetric static fission path is determined by a fixed neck radius $R_{\rm neck} = 1.16$ fm, which is related to -10 MeV in the energy curve in Fig. 4 at point (C). When describing fission in the q_2-q_3 collective space, scission is characterized by a discontinuity between the two domains of prescissioned and postscissioned configurations. In the current work, the scission lines for $^{232–238}$U isotopes are described by considering both the neck radius $R_{\rm neck}$ (in the region of 1.0–1.2 fm) as well as the total kinetic energy (TKE). The total kinetic energy for a particular pair of the fragments is evaluated in the point-charge approximation of the Coulomb interaction energy between the fragments $E_{\rm TKE} = e^2 Z_H Z_L / R_{12}$. e is the proton charge, Z_H (Z_L) is the charge of the heavy (light) fragment, and R_{12} is the distance between fragment centers of charge at scission. The TKEs shown in Fig. 6 correspond to the fragment masses $A_f(q_2, q_3)$ evaluated for each U isotope separately along its scission-line on the plane $(q_2, q_3; q_4)$. The consistency between the experimental and the theoretical results shown in Fig. 6 indicates that the present model describes the mean value of the total kinetic energy of these nuclei rather well. It is observed that the neck radius $R_{\rm neck}$ and the total kinetic energy may be suitable to describe the scission configuration based on the present model. According to the above results, the scission configuration of ^{236}U calculated by the present model is shown in Fig. 7.

Moreover, as shown in Fig. 8, we calculate the pairing energy $E^{\nu(\pi)}_{\rm pair}$ with different pairing interaction strengths G from 80% to 140% along the scission configuration in Fig. 7. The model calculations show that the pairing energy magnitudes at the asymmetric scission point (C) and symmetric scission point (D) grow faster with the variation of the pairing interaction strength. It reveals that the asymmetric and symmetric scission points seem sensitive to the variation of the pairing interaction strength G. Similar results for ^{240}Pu are provided by using the HFB method in Ref. [19]. The consistent behavior shown in Figs. 5 and 8 demonstrate that the pairing interaction strength may play a crucial role in the scission region of ^{236}U under the present model.

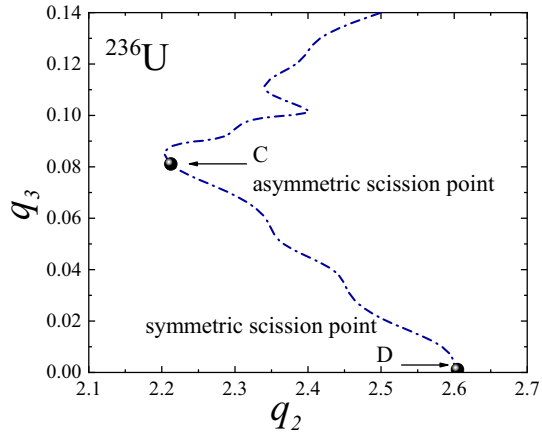

FIG. 7. The scission configuration of ^{236}U in the q_2-q_3 plane.

B. Impact of pairing on the mass distribution

The dynamics around the scission configuration are crucial to understand many aspects of the final fission state, including the mass, TKE, and the odd-even effects in mass distributions [7,8,37,50]. Figure 9 presents the results of our calculations for the odd-even mass difference of ^{236}U in the asymmetric and symmetric scission points with different pairing interaction strengths G. The corresponding experimental values of nuclei obtained by Eq. (9) with masses around 140, 96 (asymmetric scission fragment), and 118 (symmetric scission fragment), respectively, are shown for comparison. One assumes here that the ground-state odd-even mass differences represent the odd-even binding-energy differences in the scission configuration, despite some differences in the shapes. It is clearly shown that the calculations with 120% pairing interaction strength at the asymmetric scission point (C) reproduce well the experimental data. On the other hand, for the symmetric scission point (D), a stronger pairing interaction

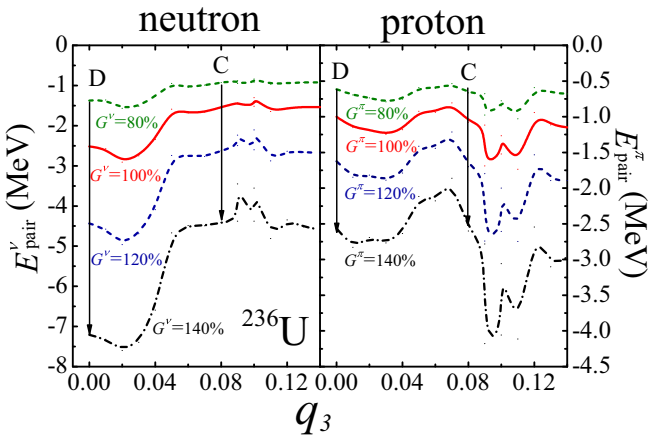

FIG. 8. Neutron and proton pairing interaction energy $E^{\nu(\pi)}_{\rm pair}$ calculated from Eq. (1), as functions of q_3 along the scission configuration with different pairing interaction strength $G^{\nu(\pi)}$ (in MeV) for ^{236}U. (C), (D) indicate the asymmetric scission point and the symmetric scission point. The arrows show the gap between the $E^{\nu(\pi)}_{\rm pair}$ values with different G^ν (G^π) values (in MeV).

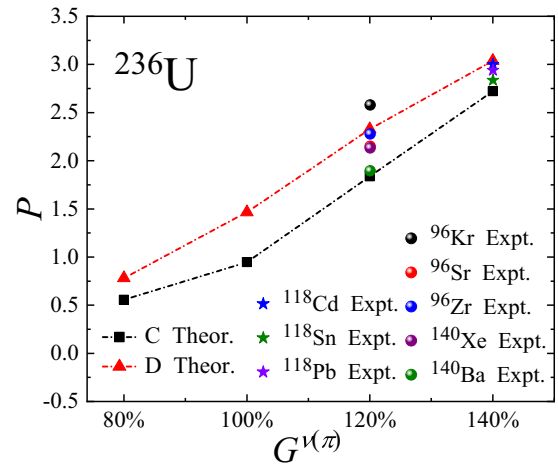

FIG. 9. The odd-even mass differences (in MeV) of ^{236}U at the asymmetric scission point (C) and the symmetric scission point (D) with different pairing interaction strengths G^ν and (G^π) varied from 80% to 140% (in MeV). The theoretical values calculated in the present model based on the Eq. (20) in Ref. [58] are denoted as "Theor." The experimental values of the odd-even mass difference for ^{96}Kr, ^{96}Sr, ^{96}Zr, ^{140}Xe, ^{140}Ba, ^{118}Cd, ^{118}Sn, and ^{118}Pd denoted as "Expt." are taken from Ref. [60] (in MeV).

strength (120%–140%) is required to generate a better pairing interaction. The mass yields $Y(q_3)$ of the $^{233-236}$U, and ^{238}U isotopes are calculated according to Eq. (23) with the pairing interaction strength parameters $G^\nu = 0.096$ MeV and $G^\pi = 0.120$ MeV (120% pairing interaction strength). As shown in Fig. 10, the mass yields of the $^{233-238}$U isotopes calculated by the present model are systematically close to the corresponding experimental values. The preneutron experimental data for $^{234-236}$U are used in Fig. 10. For ^{238}U, the postneutron data are plotted just to get a piece of information about the experimental situation. The theoretical mass yields are convoluted with a Gaussian folding function of FWHM = 4.9 u [72]. These results indicate that the current model can describe the main features of the fragment mass yields in U isotopes.

Moreover, to gain insight into the possible impact of pairing interactions in mass distributions described under the present model, the mass yields of ^{236}U as a function of mass numbers (A_f) with the variation of the pairing interaction strengths are studied. Figure 11 shows that the asymmetric fission dominates the mass yields with peaks at ($A_f \approx 96$) and ($A_f \approx 140$). By varying the pairing strength G from 80% to 140%, the two asymmetric peaks of the theoretical mass yields become lower; meanwhile, the symmetric valley is enhanced. Similar results also be produced by the 3D Langevin model for ^{235}U $+n_{th}$ in Ref. [73]. The apparent changes of the peak-to-valley ratio in the mass distribution by varying the pairing interaction strength in Fig. 11 are consistent with changes in the pairing interaction energies along the scission configurations in Fig. 7. The results demonstrate that the mass distribution is sensitive to the characteristics of scission configuration [7], and the pairing interaction plays a crucial role in achieving the scission process under the current work. It is also interesting to compare our results with the calculations

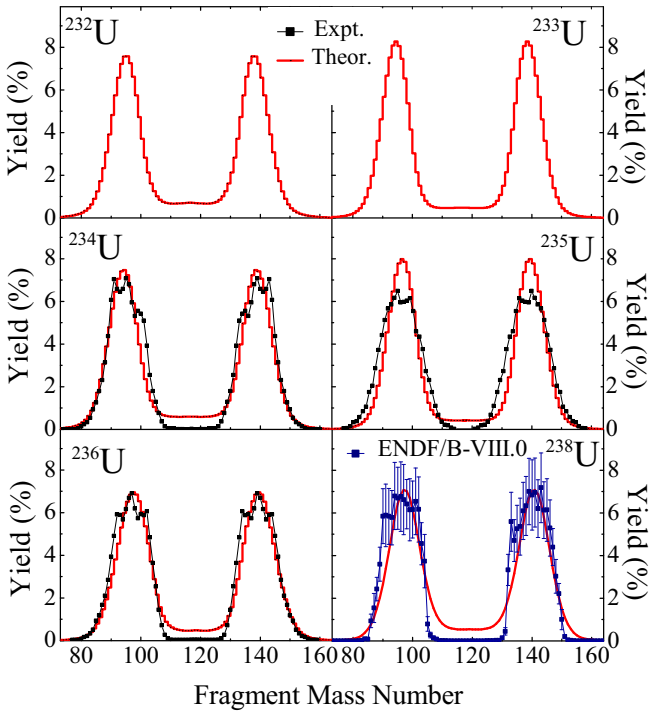

FIG. 10. The mass yield as a function of fragment mass for $^{232–236}$U, and ^{238}U. Theoretical values calculated in the present model are denoted as "Theor." Experimental data of thermal neutron induced fission are denoted as "Expt." for ^{234}U, ^{236}U [74], while, for ^{235}U, experimental data denoted as "Expt." are obtained from 0.2 MeV + ^{234}U fission [69]. To guide the eye, for ^{238}U, we use the evaluated postneutron data taken from ENDF/B-VIII.0 [75].

of ^{226}Th using the self-consistent relativistic energy density functionals + BCS framework [31]. As shown in Ref. [31], the scission points on the static fission path do not change significantly with the variation of the pairing interaction strength, which is different from our results. The charge distribution provided in Ref. [31] exhibits that the increasing static pairing interaction reduces the asymmetric peaks and enhances the symmetric peak, which is consistent with the results of the mass distribution obtained in the current work. We should clarify that the systems considered in Ref. [31] (^{226}Th) and in the present work (^{236}U) are different, and the model used in Ref. [31] is more self-consistent than the current model. On the other hand, the results in this work are based on the exactly solvable pairing model, which avoids the artificial effect produced by the BCS calculation.

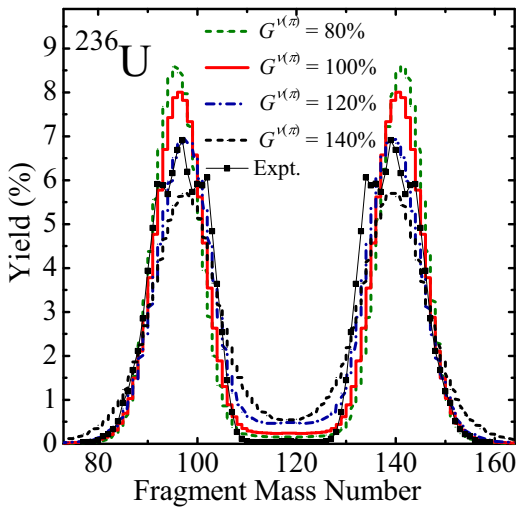

FIG. 11. The mass yields for ^{236}U as a function of mass numbers (A_f) with the variation of the pairing interaction strengths. Experimental data of thermal-neutron-induced fission denoted as "Expt." are taken from Ref. [74].

Furthermore, as shown in Fig. 11, the theoretical mass distributions with 120% pairing interaction strength yield a close agreement with the experimental data, which is consistent with the results in Figs. 9 and 10. It suggests that the pairing interaction strength in the current work should increase with the elongation of the nucleus to yield better fission products.

C. The information entropy

The microscopic mechanism of this behavior shown in Figs. 4–11 may be related to the dynamical coupling between shape and the pairing interaction [8,33]. The usual approach to show the effects of the pairing interaction is through a phenomenological analysis of the single-particle level density [55,76]. As suggested in the previous studies [33,77–79], the information (Shannon) entropy seems suitable to reveal the dynamic mechanism of this behavior in the pairing model. In Ref. [33], the analyzes of the dramatic change of the information entropy I_H and the derivative dI_H/dG at the first and second saddle points reveal that there is an intense competition between the deformation and the pairing interaction at the inner barrier and outer barrier. To confirm that the effect of the pairing interaction at the scission point at the asymmetric fission valley of ^{236}U are stronger in the present model than at the symmetric one, the information (Shannon) entropy is calculated in the four characteristic points. The information entropy is used to measure the correlations among the mean-field single-pair product states with k pairs in the ground state $|\mathrm{g}\rangle \equiv |k; x; \nu_{i'}\rangle_{\mathrm{g}}$ in Eq. (2), and it is defined as [79]

$$I_H(|\mathrm{g}\rangle) = -\sum_{i=1}^{d} |w_i|^2 \log_d(|w_i|^2), \tag{27}$$

where $\{w_i\}$ are the expansion coefficients of $|\mathrm{g}\rangle$ in terms of the mean-field single-pair product states, and d is the dimension of the space spanned by all possible single-pair product states, namely, k pairs distributed over the n levels. The information entropy I_H varies within the closed interval [0,1]. $I_H = 0$ corresponds to the case that the deformation mean field without the pairing interaction among valence nucleons dominates. When the pairing interaction is turned on, the system moves from the localized normal phase toward the delocalized superconducting (pair condensate) phase with $I_H > 0$. The most extreme situation occurs when the pairing interaction strength is sufficiently large, in which all valence nucleon pairs are most delocalized at $I_H \approx 1$.

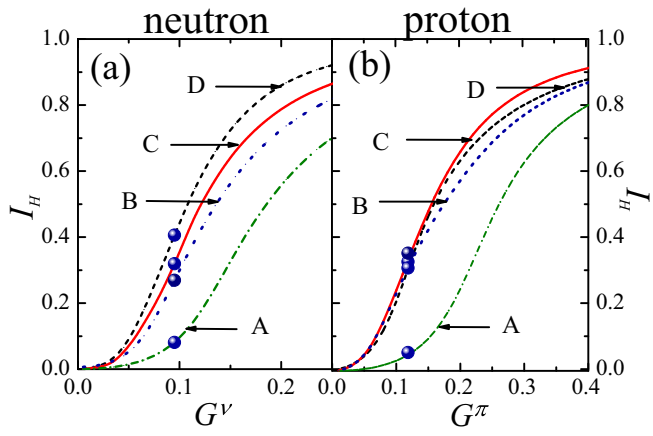

FIG. 12. The information entropy I_H for the four characteristic points of ^{236}U as functions of G^ν (G^π) (in MeV) in the present model. (A)–(D) indicate the prescission point, the scission process point, the asymmetric scission point, and the symmetric scission point, respectively. The blue balls are the realistic values of $G^\nu = 0.08$ MeV and $G^\pi = 0.10$ MeV.

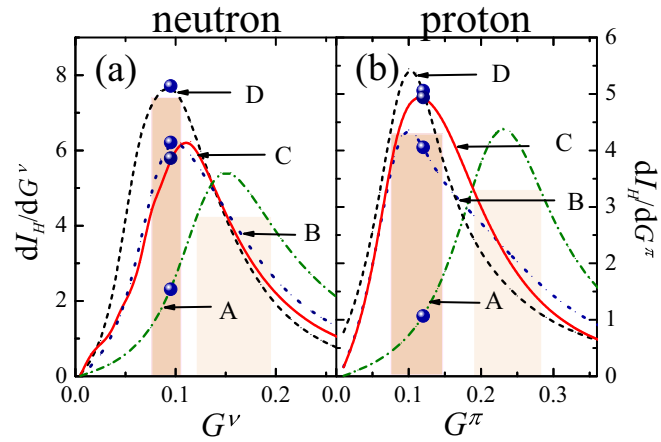

FIG. 13. The derivative of information entropy dI_H/dG for the four characteristic points of ^{236}U as functions of G^ν(G^π) (in MeV). (A)–(D) indicate the prescission point, the scission process point, the asymmetric scission point, and the symmetric scission point, respectively. The blue balls are the realistic values of $G^\nu = 0.08$ MeV and $G^\pi = 0.10$ MeV. The shadowed area indicating the width of the peak in dI_H/dG is provided to guide the eye.

As shown in Fig. 12, the values of I_H for all the four points calculated from the present model indicate that the nuclear system undergoes a rapid change from $G^\nu(G^\pi) = 0$ MeV and $I_H = 0$ to sufficiently large G^ν (G^π) = 0.24 (0.4) MeV and $I_H \approx 1$. Obviously, the variation of I_H as a function of the pairing interaction strength sketches the evolution from the deformation dominate case towards the pairing dominate case (pair condensate). Particularly, for the realistic pairing interaction around scission region with $G^\nu = 0.096$ MeV for neutron and $G^\pi = 0.12$ MeV for proton, the scission process point (B), the asymmetric scission point (C), and the symmetric point (D) are closer to dramatic change region for both neutron and proton cases. This indicates that those three points are sensitive to the variation of the pairing interaction strength. While for the prescission point (A), the system is more dominant by deformation, which means it is mainly driven by deformation and less affected by the pairing interaction. This is consistent with the results obtained from our previous work [35].

Furthermore, the derivative dI_H/dG of I_H as function of G^ν (G^π) in Fig. 13 shows the differences in those behavior more clearly. Particularly, the derivative dI_H/dG for the scission process point (B), the asymmetric scission point (C), and the symmetric point (D) reaches their maximum when G^ν and G^π equal 0.092 and 0.12 MeV, respectively. This confirms that the scission region is sensitive to the variation of the pairing interaction strength G. The differences of the derivative dI_H/dG for those points seem to be directly correlated with the behavior shown in Figs. 5 and 8, which thus provides the origin of the behavior shown in Fig. 11. Therefore, the results of the information entropy demonstrate that the pairing interaction indeed plays an important role in achieving the scission process, which thus naturally explains the origin of the behavior shown in Fig. 11 for ^{236}U in the present model.

IV. CONCLUSION

In summary, the current investigations systematically analyze the scission configurations and the mass distributions in U isotopes within the deformed mean-field plus standard pairing model. Compared with the corresponding experimental data, the systematically calculated results of the model for $^{232-236}$U isotopes, including the mass yields and TKE distributions of the fragments, reproduce the experimental data reasonably well. The magnitudes of the pairing interaction energies at the asymmetric and symmetric scission points grow faster than at the prescission points with the variation of the pairing interaction strength. Those calculations display that the asymmetric and symmetric points are much more sensitive to the variation of the pairing interaction strength than the prescission point. The apparent changes in the asymmetric peaks and symmetric valley of mass distribution with the variety of the pairing interaction strength for ^{236}U are consistent with changes in the pairing interaction energies along the scission configurations. Which confirms that the pairing interaction plays an important role in achieving the scission process for ^{236}U.

The analysis of the information entropy and its derivative dI_H/dG at the asymmetric and symmetric scission points show a strong competition between the deformation and the pairing interaction around the scission region. While, for the prescission point, the systems are more like the deform dominant case, which means the scission processes at those points are mainly driven by deformation and less affected by the pairing interaction. It thus naturally explains that the pairing interaction plays a crucial role in achieving the scission process. The model calculations also suggest that the pairing interaction strength in the current work should increase with the elongation of the nucleus in order to yield better fission products.

In particular, the present studies provide an accurate description of pairing interactions on nuclear fission, which avoids the artificial effects produced by the BCS calculation [19,31,73]. In contrast to the previous results in Ref. [31], our studies demonstrate more consistent effects of pairing interaction on the scission configurations, the total kinetic energy, and the mass distributions in U isotopes. However, the analysis shown in this work is based on the deformed mean-field plus standard pairing model, in which possible residual interactions between protons and neutrons are neglected. It should be interesting to explore the role of the interactions between protons and neutrons in the fission process.

ACKNOWLEDGMENTS

The present research was primarily supported by NSFC (12275115). The support from the NSFC (11790325,12175097), the Chinese-Polish joint project financed by the NSFC (11961131010) and the NSC of Poland (2018/30/Q/ST2/00185), and the educational department of Liaoning province (LJKMZ20221410) are also acknowledged.

The authors would like to thank Zhu-Xia Li and Xi-Zhen Wu for making constructive comments, P. Mehdipour Kaldiani for supplying us with part of the experimental data, and Yu-Xiang Wang for proofreading.

[1] M. Bender, R. Bernard, G. Bertsch, S. Chiba, J. Dobaczewski, N. Dubray, S. A. Giuliani, K. Hagino, D. Lacroix, Z. P. Li, Magierski, J. Maruhn, W. Nazarewicz, J. Pei, S. Péru, N. Pillet, J. Randrup, D. Regnier, P.-G. Reinhard, L. M. Robledo, W. Ryssens, J. Sadhukhan, G. Scamps, N. Schunck, C. Simenel, J. Skalski, I. Stetcu, P. Stevenson, S. Umar, M. Verriere, D. Vretenar, M. Warda, and S. Åberg, J. Phys. G **47**, 113002 (2020).
[2] A. Bulgac, Phys. Rev. C **102**, 044609 (2020).
[3] A. Bulgac, P. Magierski, K. J. Roche, and I. Stetcu, Phys. Rev. Lett. **116**, 122504 (2016).
[4] J. Zhao, T. Nikšić, D. Vretenar, and S.-G. Zhou, Phys. Rev. C **101**, 064605 (2020).
[5] J. C. Pei, W. Nazarewicz, J. A. Sheikh, and A. K. Kerman, Phys. Rev. Lett. **102**, 192501 (2009).
[6] K. H. Schmidt and B. Jurado, Rep. Prog. Phys. **81**, 106301 (2018).
[7] N. Schunck and L. M. Robledo, Rep. Prog. Phys. **79**, 116301 (2016).
[8] G. F. Bertsch, W. Younes, and L. M. Robledo, Phys. Rev. C **97**, 064619 (2018).
[9] G. F. Bertsch and L. M. Robledo, Phys. Rev. C **100**, 044606 (2019).
[10] J.-F. Lemaître, S. Goriely, S. Hilaire, and J.-L. Sida, Phys. Rev. C **99**, 034612 (2019).
[11] M. Caamaño, F. Farget, O. Delaune, K.-H. Schmidt, C. Schmitt, L. Audouin, C.-O. Bacri, J. Benlliure, E. Casarejos, X. Derkx, B. Fernández-Domínguez, L. Gaudefroy, C. Golabek, B. Jurado, A. Lemasson, D. Ramos, C. Rodríguez-Tajes, T. Roger, and A. Shrivastava, Phys. Rev. C **92**, 034606 (2015).
[12] M. V. Borunov, P. N. Nadtochy, and G. D. Adeev, Nucl. Phys. A **799**, 56 (2008).
[13] M. Verriere, N. Schunck, and T. Kawano, Phys. Rev. C **100**, 024612 (2019).
[14] M. Verriere and M. R. Mumpower, Phys. Rev. C **103**, 034617 (2021).
[15] W. Nazarewicz, Nucl. Phys. A **557**, 489 (1993).
[16] T. Nakatsukasa and N. R. Walet, Phys. Rev. C **57**, 1192 (1998).
[17] M. Mirea, Eur. Phys. J. A **51**, 36 (2015).
[18] M. Mirea and R. C. Bobulescu, J. Phys. G **37**, 055106 (2010).
[19] N. Schunck, D. Duke, H. Carr, and A. Knoll, Phys. Rev. C **90**, 054305 (2014).
[20] S. A. Giuliani and L. M. Robledo, Phys. Rev. C **88**, 054325 (2013).
[21] M. G. Urin and D. F. Zaretsky, Nucl. Phys. **75**, 101 (1966).
[22] L. G. Moretto and R. P. Babinet, Phys. Lett. B **49**, 147 (1974).
[23] T. Ledergerber and H.-C. Pauli, Nucl. Phys. A **207**, 1 (1973).
[24] A. Staszczak, A. Baran, K. Pomorski, and K. Böning, Phys. Lett. B **161**, 227 (1985).
[25] Y. A. Lazarev, Phys. Scr. **35**, 255 (1987).
[26] K. Pomorski, Int. J. Mod. Phys. E **16**, 237 (2007).
[27] G. Bertsch and H. Flocard, Phys. Rev. C **43**, 2200 (1991).
[28] Z. Łojewski and A. Staszczak, Nucl. Phys. A **657**, 134 (1999).
[29] J. Sadhukhan, J. Dobaczewski, W. Nazarewicz, J. A. Sheikh, and A. Baran, Phys. Rev. C **90**, 061304(R) (2014).
[30] Y. Qiang, J. C. Pei, and P. D. Stevenson, Phys. Rev. C **103**, L031304 (2021).
[31] H. Tao, J. Zhao, Z. P. Li, T. Nikšić, and D. Vretenar, Phys. Rev. C **96**, 024319 (2017).
[32] K. H. Schmidt and B. Jurado, Eur. Phys. J. A **51**, 176 (2015).
[33] X. Guan and C. Qi, Comput. Phys. Commun. **275**, 108310 (2022).
[34] X. Y. Liu, C. Qi, X. Guan, and Z. Liu, Comput. Phys. Commun. **263**, 107897 (2021).
[35] X. Guan, Y. Xin, Y. J. Chen, X. Z. Wu, and Z. X. Li, Phys. Rev. C **104**, 044329 (2021).
[36] C. Schmitt, K. Pomorski, B. K. Nerlo-Pomorska, and J. Bartel, Phys. Rev. C **95**, 034612 (2017).
[37] K. Pomorski, A. Dobrowolski, R. Han, B. Nerlo-Pomorska, M. Warda, Z. G. Xiao, Y. J. Chen, L. L. Liu, and J. L. Tian, Phys. Rev. C **101**, 064602 (2020).
[38] L. L. Liu, Y. J. Chen, X. Z. Wu, Z. X. Li, Z. G. Ge, and K. Pomorski, Phys. Rev. C **103**, 044601 (2021).
[39] R. W. Richardson, Phys. Lett. **3**, 277 (1963); **5**, 82 (1963); R. W. Richardson and N. Sherman, Nucl. Phys. **52**, 221 (1964); **52**, 253 (1964).
[40] M. Gaudin, J. Phys. (Paris) **37**, 1087 (1976).
[41] F. Pan, J. P. Draayer, and W. E. Ormand, Phys. Lett. B **422**, 1 (1998).
[42] J. Dukelsky, C. Esebbag, and S. Pittel, Phys. Rev. Lett. **88**, 062501 (2002); J. Dukelsky, S. Pittel, and G. Sierra, Rev. Mod. Phys. **76**, 643 (2004).
[43] A. Faribault, O. El Araby, C. Sträter, and V. Gritsev, Phys. Rev. B **83**, 235124 (2011); O. El Araby, V. Gritsev, and A. Faribault, *ibid.* **85**, 115130 (2012).
[44] X. Guan, K. D. Launey, M. X. Xie, L. Bao, F. Pan, and J. P. Draayer, Comput. Phys. Commun. **185**, 2714 (2014).
[45] C. Qi and T. Chen, Phys. Rev. C **92**, 051304(R) (2015).
[46] X. Guan, K. D. Launey, M. X. Xie, L. Bao, F. Pan, and J. P. Draayer, Phys. Rev. C **86**, 024313 (2012).

[47] R. W. Hasse and W. D. Myers, *Geometrical Relationships of Macroscopic Nuclear Physics* (Spinger-Verlag, Berlin, 1988).
[48] B. Nerlo-Pomorska, K. Pomorski, and F. A. Ivanyuk, Acta Phys. Pol. B Proc. Suppl. **8**, 659 (2015).
[49] K. Pomorski, F. A. Ivanyuk, and B. Nerlo-Pomorska, Eur. Phys. J. A **53**, 59 (2017).
[50] K. Pomorski, B. Nerlo-Pomorska, J. Bartel, and C. Schmitt, EPJ Web Conf. **169**, 00016 (2018).
[51] K. Pomorski, J. M. Blanco, P. V. Kostryukov, A. Dobrowolski, B. Nerlo-Pomorska, M. Warda, Z. G. Xiao, Y. J. Chen, L. L. Liu, J. L. Tian, X. Y. Diao, and Q. H. Wu, Chin. Phys. C **45**, 054109 (2021).
[52] J. Randrup, S. E. Larsson, P. Möller, S. G. Nilsson, K. Pomorski, and A. Sobiczewski, Phys. Rev. C **13**, 229 (1976).
[53] K. Pomorski and J. Dudek, Phys. Rev. C **67**, 044316 (2003).
[54] P. Moller, J. R. Nix, W. D. Myers, and W. J. Swiatecki, At. Data Nucl. Data Tables **59**, 185 (1995).
[55] V. M. Strutinsky, Nucl. Phys. A **95**, 420 (1967).
[56] V. M. Strutinsky, Nucl. Phys. A **122**, 1 (1968).
[57] Y. Sun, Phys. Scr. **91**, 043005 (2016).
[58] M. Bender, K. Rutz, P.-G. Reinhard, and J. A. Maruhn, Eur. Phys. J. A **8**, 59 (2000).
[59] K. Pomorski and F. A. Ivanyuk, Int. J. Mod. Phys. E **18**, 900 (2009).
[60] U. S. National Nuclear Data Center, http://www.nndc.bnl.gov/.
[61] M. Samyn, S. Goriely, and J. M. Pearson, Phys. Rev. C **72**, 044316 (2005).
[62] S. E. Agbemava, A. V. Afanasjev, and P. Ring, Phys. Rev. C **93**, 044304 (2016).
[63] R. Capote *et al.*, Nucl. Data Sheets **110**, 3107 (2009).
[64] A. J. Sierk, Phys. Rev. C **96**, 034603 (2017).
[65] K. Rutz, M. Bender, P. Reinhard, and J. A. Maruhn, Phys. Lett. B **468**, 1 (1999).
[66] J. D. McDonnell, W. Nazarewicz, and J. A. Sheikh, Phys. Rev. C **87**, 054327 (2013).
[67] Y. J. Chen, S. Yang, G. X. Dong, L. L. Liu, Z. G. Ge, and X. B. Wang, Chin. Phys. C **46**, 024103 (2022).
[68] M. Asghar, F. Caitucoli, B. Leroux, P. Perrin, and G. Barreau, Nucl. Phys. A **368**, 328 (1981).
[69] A. Al-Adili, F.-J. Hambsch, S. Pomp, S. Oberstedt, and M. Vidali, Phys. Rev. C **93**, 034603 (2016).
[70] P. M. Kaldiani, Phys. Rev. C **102**, 044612 (2020).
[71] F. Vives, F.-J. Hambsch, H. Bax, and S. Oberstedt, Nucl. Phys. A **662**, 63 (2000).
[72] A. Göök, F.-J. Hambsch, S. Oberstedt, and M. Vidali, Phys. Rev. C **98**, 044615 (2018).
[73] K. Pomorski and B. Nerlo-Pomorska, Acta Phys. Pol. B Proc. Suppl. **163**, 4-A21 (2023).
[74] P. Geltenbort, F. Goennenwein, and A. Oed, Conf. Nucl. Data Basic Appl. Sci. **1**, 393 (1985).
[75] K.-H. Schmidt, B. Jurado, C. Amouroux, and C. Schmitt, Nucl. Data Sheets **131**, 107 (2016).
[76] S. Karatzikos, A. V. Afanasjev, G. A. Lalazissis, and P. Ring, Phys. Lett. B **689**, 72 (2010).
[77] X. Guan, K. D. Launey, J. Z. Gu, F. Pan, and J. P. Draayer, Phys. Rev. C **88**, 044325 (2013).
[78] Y. Yue, Y. J. Chen, and X. Guan, Eur. Phys. J. A **56**, 164 (2020).
[79] A. Volya and V. Zelevinsky, Phys. Lett. B **574**, 27 (2003).